minerals

Article

Mineralogical, Geochronological, and Geochemical Characteristics of Early Cretaceous Granite in South China: Implications for Tectonic Evolution and REE Mineralization

Yue Qin [1], Yongfeng Cai [1,2], Wei Fu [1], Zhixuan Han [1], Panfeng Liu [1], Changling Lao [1], Yongshan Zhao [1], Zhengchao Han [1] and Yun Zhou [1,*]

1 Guangxi Key Laboratory of Hidden Metallic Ore Deposits Exploration, College of Earth Sciences, Guilin University of Technology, Guilin 541004, China
2 Collaborative Innovation Center for Exploration of Hidden Nonferrous Metal Deposits and Development of New Materials in Guangxi, Guilin University of Technology, Guilin 541004, China
* Correspondence: zhouyun@glut.edu.cn

Abstract: One of the most important geological features of South China are the widespread Mesozoic igneous rocks that play a key role in revealing the tectonic evolution of South China. Due to the thick covering of vegetation and Quaternary sediments, the early Cretaceous magmatism in southwestern South China is still not well constrained. In this paper, we report newly identified early Cretaceous granites in Guangxi, South China. Zircon U–Pb dating results showed that representative fine-grained and coarse-grained granites in northeastern Guangxi indicate the early Cretaceous ages of 141 ± 3 Ma and 141 ± 4 Ma, respectively. Geochemically, both fine-grained and coarse-grained granites had high 10,000 × Ga/Al ratios and belonged to A-type granite. They had undergone high degrees of magma differentiation, as evidenced by extremely negative Sr, Ba, and Eu anomalies. They had high REE (rare earth elements) contents (>451 ppm). The fine-grained granites were characterized by higher HREE (heavy rare earth elements) contents, lower LREE (light rare earth elements) contents, and lower LREE/HREE ratios than the coarse-grained granites. Integrated with regional geological data, the early Cretaceous granites were likely formed in a back-arc extensional environment in response to the increased subduction angle of the Paleo-Pacific plate. Different REE contents in the fine- and coarse-grained granites may be a result of fractional crystallization. Magma differentiation and hydrothermal alteration might have played an important role in REE mineralization of the early Cretaceous granites in Guangxi.

Keywords: early Cretaceous granites; zircon U-Pb geochronology; REE mineralization; Paleo-Pacific plate; Xinlu pluton

Citation: Qin, Y.; Cai, Y.; Fu, W.; Han, Z.; Liu, P.; Lao, C.; Zhao, Y.; Han, Z.; Zhou, Y. Mineralogical, Geochronological, and Geochemical Characteristics of Early Cretaceous Granite in South China: Implications for Tectonic Evolution and REE Mineralization. *Minerals* **2022**, *12*, 1308. https://doi.org/10.3390/min12101308

Academic Editor: Clemente Recio

Received: 6 September 2022
Accepted: 14 October 2022
Published: 17 October 2022

1. Introduction

The South China Craton, located in Southeast China at the West Pacific, is characterized by widespread Mesozoic igneous rocks (Figure 1, [1–3]). These igneous rocks provide important geological records to decipher the Mesozoic geodynamic mechanism of the South China Craton. Previous studies have shown that oblique subduction of the Paleo-Pacific plate underneath South China occurred during Late Permian to Early Triassic, as evidenced by the 254–242 Ma alkaline syenites from the eastern part of the South China Craton [4]. Some workers argued that initial subduction of the Paleo-Pacific plate beneath South China took place during the Early Jurassic [5]. In addition, flat-slab subduction of the Paleo-Pacific plate and subsequent foundering or break-off of the flat slab was proposed to explain the large-scale and long-term Mesozoic magmatism in the South China Craton [6]. According to magmatism and tectonic records from the southeast coastal areas of China and other areas in the East Asia, some studies have further suggested that the drifting direction of the Paleo-Pacific plate had changed several times since early Cretaceous (ca.

140 Ma) [7–10]. However, it remains unclear as to whether or when the drifting direction of the Paleo-Pacific plate occurred in the inland areas of South China because of a lack of early Cretaceous magmatism.

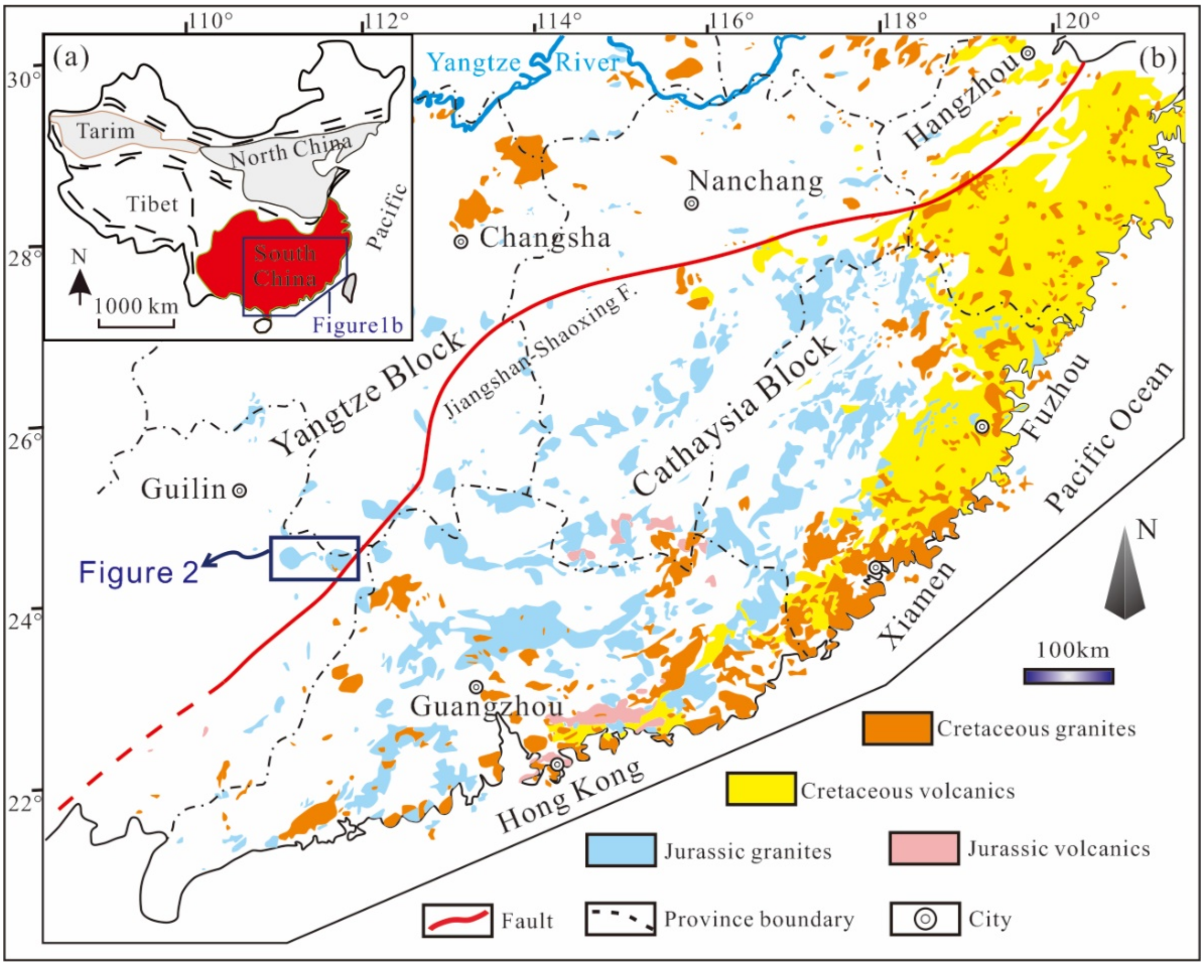

Figure 1. Simplified geological map showing the location of South China (**a**), and distribution of the Mesozoic igneous rocks in South China (**b**).

The Huashan–Guposhan granitic pluton, located in the northeastern Guangxi Zhuang Autonomous Region, is an important part of the Mesozoic igneous rocks in the South China Craton. Previous studies have shown that the major formation age of the pluton is Jurassic [11–16]. Our study has identified early Cretaceous granites in this pluton. This provides new evidence to constrain the Mesozoic tectonic evolution of the South China Craton. Therefore, in this study, we provide laser ablation inductively coupled mass spectrometry (LA–ICP–MS) zircon U-Pb ages, as well as whole-rock major- and trace-element contents, alongside chemical composition of biotites for newly identified early Cretaceous granites in the Huashan–Guposhan area. Furthermore, we integrated our results with analysis of the previous Mesozoic geological data in the South China Craton to discuss the petrogenetic type of the granite, the geodynamics derived by the subduction of Paleo-Pacific plate, and the relationship between granitic magmatism and REE mineralization.

2. Regional Geological Setting

The South China Craton is composed of the Cathaysia Block in the southeast and Yangtze Block in the northwest. The two blocks were amalgamated along the Jiangnan orogen during the Neoproterozoic, as evidenced by widespread Neoproterozoic igneous rocks in the South China Craton [17–19]. After that, the South China Craton underwent multiple Phanerozoic tectonic events, as recorded by large volumes of Kwangsian (early Paleozoic), Indosinian, and Yanshanian igneous rocks and deformations [20–24].

Tectonically, the Huashan–Guposhan granitic pluton is located at the joining part of Cathaysia and Yangtze blocks (Figure 1). The Huashan–Guposhan granitic pluton, covering an area of approximately 1300 km^2, is a composite pluton that is composed of the Huashan pluton, Niumiao pluton, and Tong'an pluton in the west and Guposhan pluton, Lisong pluton, Yinping pluton, Wuyangshan pluton, and Xinlu pluton in the east (Figure 2; [25–27]). Large-scale W-Sn polymetallic mineralization is intimately associated with the above plutons [13,28–30]. In addition, the Huashan–Guposhan pluton mainly intruded into the Cambrian, Devonian, and Carboniferous strata. The formation of skarns, hornhelses, and marbles are common in the surrounding rocks [31].

Sediments in the studied area are mainly Cambrian, Devonian, Carboniferous, and Jurassic (Figure 2). The Cambrian mainly consists of sandy shales of neritic facies interbedded with lenses of limestone. The thickness of the Cambrian is more than 3000 m. The Devonian, showing a thickness greater than 3500 m, is in angular unconformable contact with the underlying Cambrian. The lower Devonian is mainly composed of purple-red sandstone and gray-black sandy shale. The northern part of the upper Devonian is a suite of carbonates that is mainly composed of medium-thick limestones, muddy limestones, and dolomitic limestones, whereas the southern part of the upper Devonian mainly consists of siliceous rocks. The lower Carboniferous mainly consists of dark gray dolomites, dolomitic limestones, and limestones with a thickness greater than 200 m. The middle Carboniferous, more than 540 m in thickness, is mainly composed of yellow calcareous shales and gray-black cherty limestones, whereas the upper Carboniferous is mainly composed of light gray dolomites and gray-white limestones with a thickness greater than 200 m. The Carboniferous is in conformable contact with the underlying Devonian. The Jurassic is mainly composed of purple-red breccia, manganese shale, siltstone, shale, and argillaceous sandstone with a thickness more than 460 m [32,33].

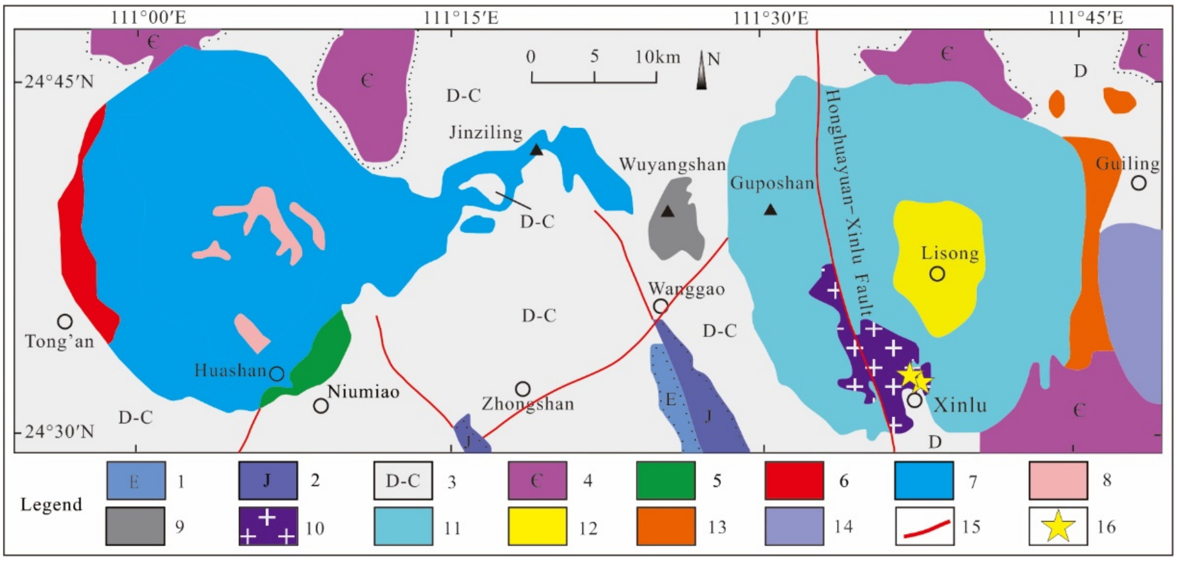

Figure 2. Schematic geological map showing the Xinlu pluton and its surrounding areas in northeastern Guangxi. 1—Palaeogene; 2—Jurassic; 3—Devonian–Carboniferous; 4—Cambrian; 5—Niumiao pluton; 6—Tongan pluton; 7—Huashan pluton; 8—Yinping pluton; 9—Wuyangshan pluton; 10—Xinlu pluton; 11—Guposhan pluton; 12—Lisong pluton; 13—Guiling pluton; 14—Daning pluton; 15—fault; 16—sampling location.

The major fault in the study area is the NNW-trending Honghuayuan–Xinlu Fault, which extends over 100 km and cuts through the Devonian–Carboniferous strata and

Guposhan and Xinlu plutons (Figure 2). Cataclastic, folded, and silicified zones are common in the fault zone [34,35].

Weathering crusts, with a thickness of 2–60 m, are well-developed in the Huashan–Guposhan area. They are generally composed of thick regolith and a small number of exposed bedrocks. Ion-adsorption REE deposits are widespread in the Huashan–Guposhan area [36]. The type of these REE deposits is mainly LREE deposit. REE contents of the weathering crust can reach up to 2365 ppm [36].

The Xinlu pluton studied in this paper is located in the southeastern part of the Huashan–Guposhan pluton (Figure 2) and is about 48 km^2 in area. Samples HZ12A and HZ13A were collected from Xinlu pluton. The sample HZ12A is a fine-grained biotite granite (Figure 3a) and is mainly composed of quartz (around 45%), plagioclase (around 35%), K-feldspar (around 10%), and biotite (around 10%). The accessory minerals are mainly sphene, zircon, apatite, chlorite, epidote, magnetite, and ilmenite. The quartz shows melting corrosion structure (Figure 3c). The sample HZ13A is coarse-grained porphyritic potassium granite (Figure 3b) and mainly consists of quartz (around 45%), K-feldspar (around 25%), plagioclase (around 20%), and biotite (around 10%). The accessory minerals include zircon, apatite, magnetite, and ilmenite. The plagioclase and k-feldspar always contains inclusions of quartz. The K-feldspar is brown, due to alteration, and shows two directions of cleavage (Figure 3d). The quartz shows rounded margins (Figure 3d). The biotite always alters to chlorite and epidote (Figure 3c).

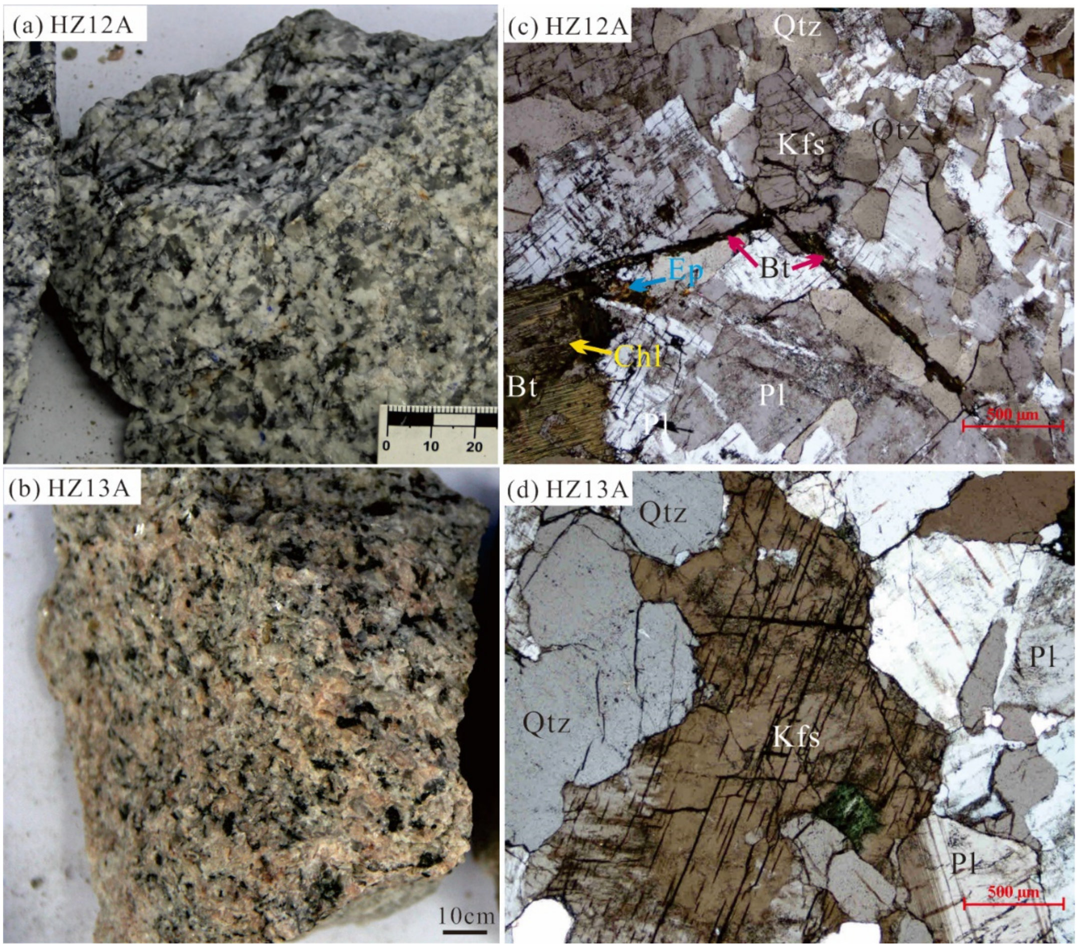

Figure 3. Field photos and photomicrographs of representative samples from Xinlu pluton. Pl: plagioclase. Kfs: K-feldspar. Qtz: quartz. Bt: biotite. Chl: chlorite. Ep: epidote. (**a**) Field photos of fine-grained biotite granite, (**b**) field photos of coarse-grained porphyritic potassium granite, (**c**) photomicrographs of fine-grained biotite granite, and (**d**) photomicrographs of coarse-grained porphyritic potassium granite.

3. Analytical Methods

Zircons separated from samples HZ12A and HZ13A for U-Pb analyses were conducted by conventional heavy liquid and magnetic techniques, and were further hand-picked under binocular microscope. The hand-picked zircon grains, together with standard sample (Temora), were mounted in epoxy resins. Finally, we polished and sectioned the zircon grains in half for analysis. Zircon U-Pb analyses were performed using laser ablation multiple collector inductively coupled plasma mass spectrometry (LA–MC–ICP–MS) at the Guangxi Key Laboratory of Hidden Metallic Ore Deposits Exploration, Guilin University of Technology. Sample mounts were placed in a two-volume sample cell flushed with Ar and He. Laser ablation was operated at a constant energy of 80 mJ and at 8 Hz, with a spot diameter of 32 μm. The ablated material was carried by He gas to the Agilent 7500cx ICP–MS. Element corrections were made for mass bias drift, which was evaluated by reference to standard glass NIST 610 [37]. The zircon Temora was used as the age standard ($^{206}Pb/^{238}U$ = 416.8 Ma) [38]. The detailed analytical procedure followed [39]. $^{207}Pb/^{206}Pb$ and $^{206}Pb/^{238}U$ ratios were calculated using the ICPMSDataCal8.0 [40] and were then corrected using zircon GJ-1 as the external standard. The $^{207}Pb/^{235}U$ ratios were calculated from the values of $^{207}Pb/^{206}Pb$ and $^{206}Pb/^{238}U$. Apparent U-Pb ages were computed by the Isoplot program [41].

The collected samples were sawed into slabs, and the central fresh parts were selected for pulverizing to 200-mesh in preparation for elemental analyses. Major oxide for whole rocks was analyzed by wavelength X-ray fluorescence spectrometry using a Rigaku ZSX Primus II spectrometer (Tokyo, Japan) with the relative standard deviations of <5%. Glass discs were made by melting dehydrated sample powders. Calibration lines used in quantification were produced by bivariate regression of data from 36 reference materials encompassing a large range of silicate compositions [42]. Trace element concentrations were measured using an Agilent 7500cx (Santa Clara, CA, USA) inductively coupled plasma mass spectrometer (ICP-MS). The specified sample preparation and analytical method were based on [43]. An internal standard solution containing the single element Rh was used to monitor signal drift during counting. Analytical precision is typically better than 5%.

Fresh biotite from the granite samples was selected for the electron probe microanalysis. The instrument used for the electron probe microanalysis was the JXA-8230 Electron Probe Microanalyzer produced by Oxford Instruments, Oxford, UK. The analysis and test conditions were accelerating voltage of 15 kV; the current was 30 nA, and the beam spot diameter was 1 μm. The main elements tested included SiO_2, TiO_2, MgO, FeO, Na_2O, K_2O, Al_2O_3, CaO, and P_2O_5, etc. The detection limit of oxides is 0.01%.

4. Results

4.1. Geochemical Characteristics

Six samples HZ11 (24°31′20″ N, 111°36′46″ E), HZ12A (24°31′18″ N, 111°36′38″ E), HZ12B (24°31′21″ N, 111°36′23″ E), HZ13A (24°31′19″ N, 111°36′55″ E), HZ13B (24°31′25″ N, 111°36′38″ E), and HZ14 (24°31′35″ N, 111°36′05″ E) from the Xinlu pluton had 72.38–74.80 wt % of SiO_2. The coarse-grained granite samples had 0.06–0.07 wt % of TiO_2, 1.00–1.14 wt % of Fe_2O_3T (total Fe_2O_3), and 13.47–14.50 wt % of Al_2O_3, whereas the fine-grained granites showed higher TiO_2 (>0.13 wt %) and Fe_2O_3T (3.60–3.64 wt %) contents and lower Al_2O_3 (11.86–12.12 wt %) contents (Table 1). All the samples showed A/CNK values of 0.90 to 1.27, indicating they were metaluminous-peraluminous (Figure 4a). Their K_2O contents were 3.52–5.48 wt %, indicating they were high-K calc-alkaline rocks (Figure 4b). On the Harker variation diagrams, Fe_2O_3T, CaO, Na_2O, and TiO_2 had some degree of negative correlation with SiO_2, whereas MgO and P_2O_5 were relatively constant, irrespective of SiO_2 (Figure 5).

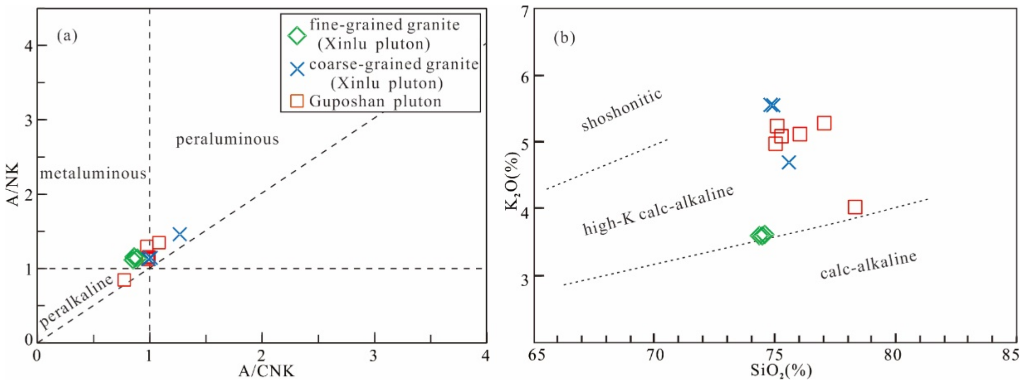

Figure 4. Plots of (**a**) A/NK versus A/CNK and (**b**) K_2O versus SiO_2 for the granites from the Xinlu and Guposhan plutons. A/NK = Al/(Na + K), A/CNK = Al/(Ca + Na + K) (molar ratio). Detailed data information is shown in Table 1.

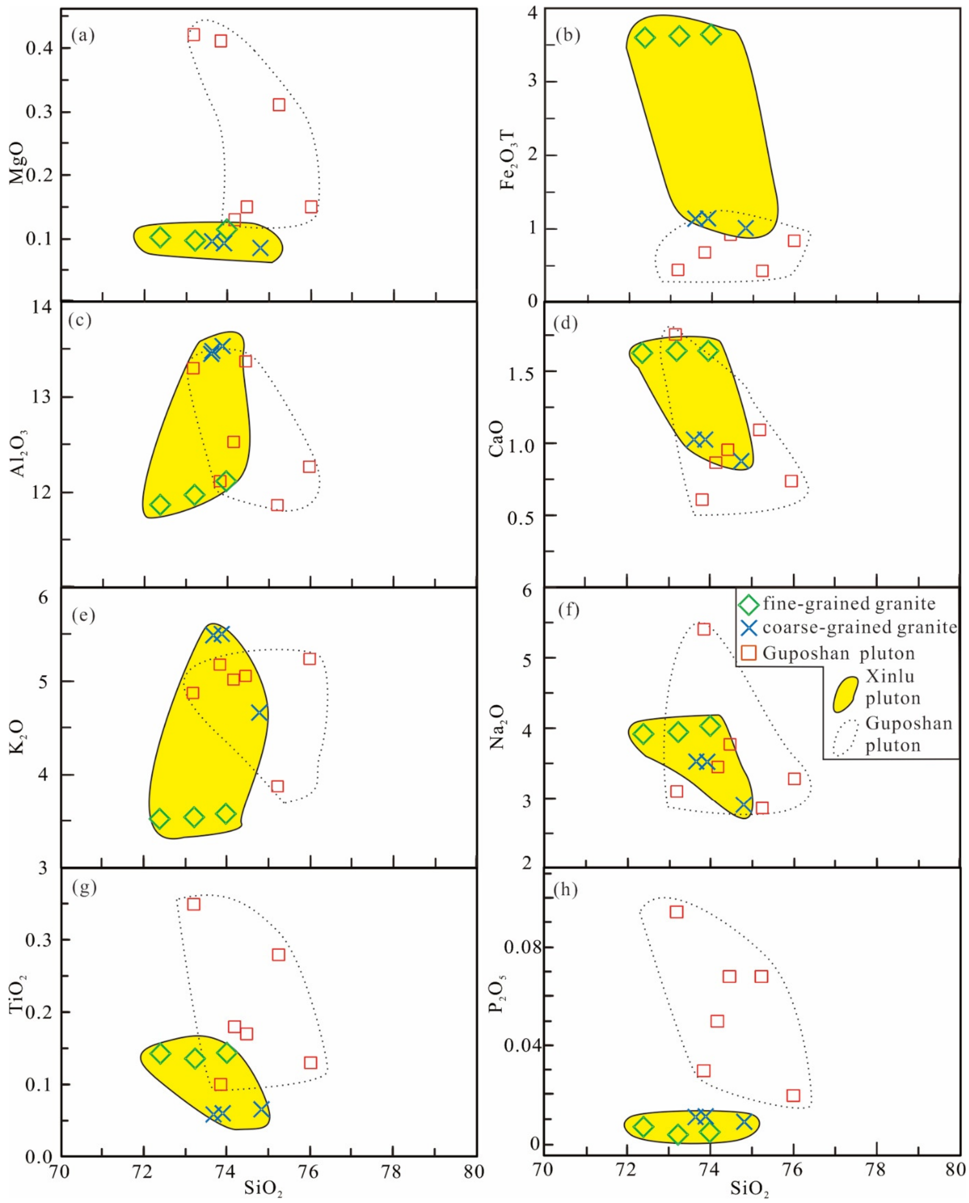

Figure 5. Plots of SiO_2 versus (**a**) MgO, (**b**) Fe_2O_3T, (**c**) Al_2O_3, (**d**) CaO, (**e**) K_2O, (**f**) Na_2O, (**g**) TiO_2, and (**h**) P_2O_5 for the granites from the Xinlu and Guposhan plutons.

Table 1. Major element (wt %) and trace element (ppm) compositions of the granite from the Xinlu and Guposhan plutons.

Pluton	Xinlu						Guposhan					
Rock Type	Fine-Grained Granite			Coarse-Grained Granite			Granite					
Sample	HZ11	HZ12A	HZ12B	HZ13A	HZ13B	HZ14	1013-1	1007-1	308	250	227	352
SiO_2	73.21	73.97	72.38	74.80	73.90	73.64	73.83	75.99	74.16	73.18	74.45	75.22
TiO_2	0.14	0.14	0.14	0.07	0.06	0.06	0.10	0.13	0.18	0.35	0.17	0.28
Al_2O_3	11.97	12.12	11.86	14.50	13.51	13.47	12.11	12.26	12.52	13.29	13.36	11.86
$Fe_2O_3{}^T$	3.62	3.64	3.60	1.00	1.14	1.14	0.68	0.84	1.16	0.44	0.92	0.43
MgO	0.10	0.11	0.10	0.09	0.09	0.10	0.41	0.15	0.13	0.42	0.15	0.31
CaO	1.65	1.65	1.64	0.88	1.03	1.03	0.61	0.74	0.87	1.77	0.96	1.10
K_2O	3.54	3.58	3.52	4.65	5.48	5.47	5.16	5.22	5.00	4.86	5.04	3.87
Na_2O	3.94	4.03	3.92	2.91	3.52	3.51	5.40	3.28	3.45	3.10	3.77	2.86
MnO	0.09	0.09	0.09	0.04	0.04	0.04	0.02	0.03	0.04	0.06	0.04	0.07
P_2O_5	/	0.01	0.01	0.01	0.01	0.01	0.03	0.02	0.05	0.09	0.07	0.07
LOI	1.10	0.54	0.74	0.82	0.44	0.76	/	/	/	0.55	0.41	1.78
Total	99.36	99.89	98.00	99.77	99.24	99.23	98.35	98.66	97.56	98.12	99.34	97.85
Ga	44.2	43.1	43.6	34.0	30.5	30.3	33.7	29.5	23.7	21.5	24.3	20.1
Rb	624	610	614	559	496	493	365	391	/	242	348	234
Sr	4.74	4.68	4.70	4.74	4.18	4.17	12.3	37.8	56.3	99.4	57.3	36.6
Zr	749	728	735	440	395	417	172	166	86.7	106	113	75.0
Nb	322	289	281	157	146	138	114	100	60.8	29.2	32.8	28.6
Cs	71.0	68.4	70.2	26.1	23.4	23.0	/	/	/	18.3	14.5	9.41
Ba	7.13	6.81	6.91	1.08	0.94	0.93	74.7	183	187	298	227	284
La	18.4	17.2	16.1	41.1	39.7	39.8	190	51.3	51.6	51.2	53.6	51.9
Ce	56.1	53.2	49.1	96.6	85.6	84.6	126	102	103	113	122	137
Pr	10.6	10.2	9.3	12.9	11.5	11.2	47.6	13.3	12.7	12.2	12.9	12.2
Nd	53.5	51.4	47.3	47.2	42.4	40.8	170	46.3	41.8	40.7	38.6	44.0
Sm	26.9	25.7	23.8	14.6	13.5	12.7	40.8	10.8	8.57	9.43	8.31	9.74
Eu	0.02	0.02	0.02	0.03	0.02	0.02	0.72	0.52	0.58	0.96	0.62	0.72
Gd	35.6	33.7	32.2	18.2	16.7	15.7	34.9	11.3	9.07	9.45	7.56	10.4
Tb	10.2	9.68	9.18	4.35	4.00	3.76	5.98	2.11	1.75	1.52	1.19	1.81
Dy	80.4	76.4	72.8	31.7	29.4	27.6	33.4	13.6	10.9	8.82	6.79	11.0
Ho	18.4	17.5	16.7	6.98	6.43	6.14	6.04	2.82	2.17	1.69	1.33	2.14
Er	64.3	61.8	58.8	22.5	20.8	20.0	15.9	8.28	6.27	4.59	3.81	5.92
Tm	11.4	11.0	10.6	3.60	3.31	3.18	2.42	1.32	0.95	0.70	0.64	0.84
Yb	81.9	79.7	75.4	23.4	21.4	20.8	14.2	8.25	5.86	4.72	4.55	5.36
Lu	12.2	11.9	11.3	3.32	3.04	3.00	1.88	1.16	0.76	0.74	0.75	0.88
Y	550	533	510	183	167	161	156	71.8	47.1	47.4	35.0	56.5
Hf	20.9	18.9	18.7	13.0	11.5	12.3	5.42	5.68	/	4.26	4.53	3.62
Ta	32.7	23.7	21.0	12.9	11.6	11.0	7.48	8.11	<10	3.54	4.74	3.58
Th	137	145	117	79.4	61.5	72.6	67.0	66.5	57.8	33.4	53.0	18.2
U	134	161	158	53.1	69.5	71.4	17.5	24.8	/	11.0	14.3	7.4
∑HREE	864	834	797	297	272	262	270	120.6	84.9	79.6	61.6	94.9
∑LREE	166	158	146	212	193	189	575	224	218	228	236	256
∑REE	1030	992	943	510	465	451	846	344	303	307	298	351
LREE/HREE	0.19	0.19	0.18	0.71	0.71	0.72	2.13	1.86	2.57	2.86	3.83	2.70
Zr + Nb + Ce + Y	1678	1603	1575	877	793	801	568	440	297	296	303	298
10,000 × Ga/Al	6.85	6.68	6.75	4.38	4.21	4.18	5.17	4.48	3.49	2.98	3.40	3.07

LOI: loss on ignition. Guposhan data are from [33].

On chondrite-normalized and multi-element primitive mantle-normalized plots (normalized values are from [44]), the samples were enriched in Rb, Th, U (Figure 6a), and REE (rare earth elements, except Eu; Figure 6b), and depleted in Ba, Sr, and Ti (Figure 6a). They were characterized by high 10,000 × Ga/Al ratios (4.18–6.85) and (Nb + Ce + Zr + Y) contents (793–1678 ppm) (Table 1), as well as extremely negative Eu anomalies (Figure 6b), with δEu ($\delta Eu = Eu/\sqrt{(Sm \times Gd)}$) less than 0.1. The fine-grained granites had HREE (heavy rare earth elements) contents of 797–864 ppm, LREE (light rare earth elements) contents of 146–166 ppm, and LREE/HREE ratios of 0.18–0.19. The coarse-grained granites had lower HREE contents (262–297 ppm), higher LREE contents (189–212 ppm), and higher LREE/HREE ratios (0.71–0.72) (Figure 6b, Table 1).

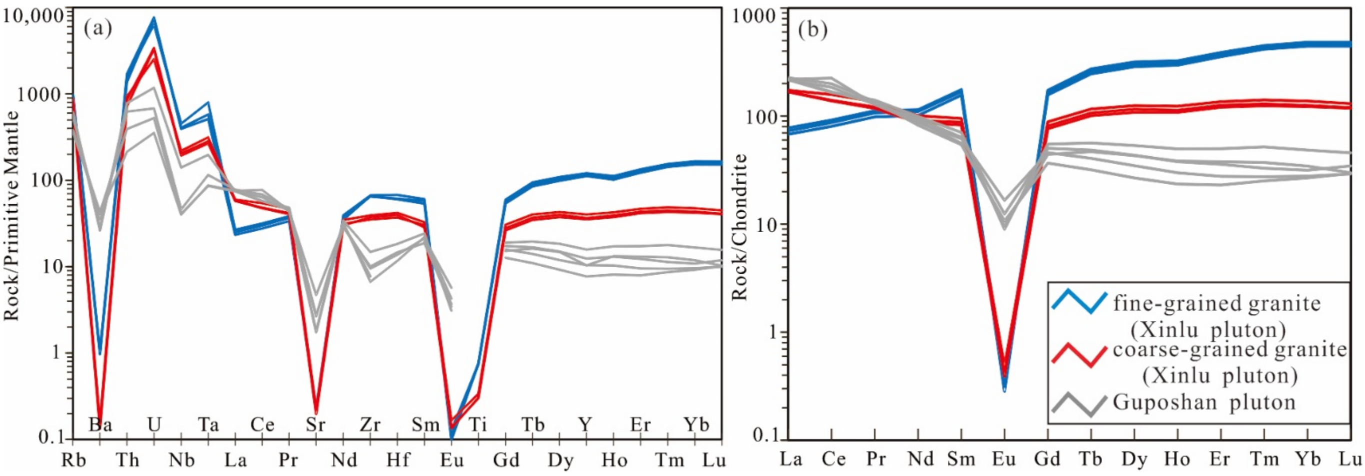

Figure 6. (**a**) Primitive-mantle-normalized trace element spidergrams and (**b**) chondrite-normalized REE patterns for the granites from the Xinlu and Guposhan plutons.

4.2. Compositions of Biotite

The chemical composition of biotites is listed in Table 2. Biotites from the fine-grained granites had TiO_2 contents of 0.94%–1.92%, Al_2O_3 contents of 14.1%–15.2%, FeO^T (total FeO) contents of 34.7%–36.4%, and MgO contents of 0.05%–0.16%. Biotites from the coarse-grained granites were characterized by lower TiO_2 contents (0.12%–1.53%) and higher Al_2O_3 (18.5%–19.3%), FeO^T (41.0%–43.8%), and MgO (0.26%–0.44%) contents (Table 2). In contrast to the biotites from the Xinlu pluton, the biotites from the Guposhan pluton showed the highest TiO_2 (2.69%–3.59%) and MgO (2.94%–3.23%) contents and lowest FeO^T (25.8%–31.1%) contents (Table 2). Biotites from both the fine-grained granites and coarse-grained granites had high I_{Fe} values (>0.98; $I_{Fe} = Fe^{2+}/(Fe^{2+} + Mg)$) and low I_{Mg} values (<0.02; $I_{Mg} = Mg/(Fe^{2+} + Mg)$), whereas the Guposhan pluton showed lower I_{Fe} values (<0.83) and higher I_{Mg} values (>0.17) (Table 2). These data indicated that the biotites from both the Xinlu and Goposhan plutons were iron-rich biotites that are similar to siderophyllite [45].

Table 2. Compositions of biotite of the granites from the Xinlu and Guposhan plutons.

Pluton	Xinlu													Guposhan					
Sample	Fine-Grained Granite								Coarse-Grained Granite					Granite					
SiO_2	34.3	34.5	34.4	34.0	34.5	33.6	34.3	33.5	34.4	34.0	33.2	34.2	34.0	35.3	32.9	35.9	31.5	34.9	36.2
TiO_2	1.01	0.94	1.03	1.04	1.07	1.21	1.92	1.54	0.35	0.39	0.53	0.44	0.12	3.00	2.81	3.38	2.69	3.32	3.59
Al_2O_3	14.9	15.2	15.0	15.0	15.0	14.9	14.4	14.1	18.7	18.5	18.7	19.3	19.0	14.3	14.5	14.4	12.9	13.5	14.1
FeO^T	35.4	35.7	35.1	35.5	35.4	36.4	34.8	34.7	43.8	43.4	41.0	42.3	42.7	29.3	31.1	29.5	25.8	30.1	30.5
MnO	0.33	0.31	0.29	0.32	0.34	0.21	0.21	0.20	0.39	0.32	0.71	0.46	0.37	0.14	0.14	0.20	0.12	0.19	0.19
MgO	0.10	0.05	0.09	0.11	0.11	0.16	0.08	0.20	0.37	0.37	0.44	0.28	0.26	2.94	3.23	3.00	3.02	3.20	3.19
CaO	0.28	0.10	0.11	0.10	0.10	0.10	0.02	0.04	0.07	0.07	0.07	0.09	0.35	0.03	0.08	0.09	0.09	0.08	0.03
Na_2O	0.15	0.08	0.12	0.11	0.09	0.12	0.07	0.27	0.14	0.11	0.13	0.12	0.08	0.26	0.16	0.17	0.20	0.18	0.10
K_2O	9.19	9.25	9.25	8.97	8.81	8.34	9.64	9.00	0.08	0.07	0.04	0.09	0.03	9.83	7.94	9.99	7.65	9.70	10.00
Total	95.9	96.5	95.7	95.4	95.7	95.3	95.7	93.8	98.6	97.6	95.0	97.6	97.1	95.0	92.8	96.6	84.0	95.3	97.9
FeO	32.8	32.9	32.3	32.7	32.3	33.4	32.0	32.2	41.5	41.1	38.7	39.9	40.4	26.2	27.9	26.1	22.4	27.2	27.1
Fe_2O_3	2.86	3.10	3.09	3.06	3.49	3.28	3.14	2.80	2.56	2.54	2.53	2.72	2.58	3.48	3.55	3.75	3.74	3.29	3.76
Si	5.89	5.89	5.91	5.87	5.90	5.82	5.90	5.89	5.61	5.60	5.57	5.59	5.60	5.92	5.68	5.91	5.91	5.88	5.90
Al^{IV}	2.11	2.11	2.09	2.13	2.10	2.19	2.10	2.11	2.39	2.40	2.43	2.41	2.40	2.08	2.33	2.09	2.09	2.12	2.10
Al^{VI}	0.91	0.95	0.94	0.92	0.93	0.84	0.81	0.81	1.20	1.20	1.27	1.31	1.28	0.73	0.63	0.70	0.76	0.57	0.60
Ti	0.13	0.12	0.13	0.13	0.14	0.16	0.25	0.20	0.04	0.05	0.07	0.05	0.02	0.38	0.37	0.42	0.38	0.42	0.44
Fe^{3+}	0.37	0.40	0.40	0.40	0.45	0.43	0.41	0.37	0.31	0.31	0.32	0.33	0.32	0.44	0.46	0.46	0.53	0.42	0.46
Fe^{2+}	4.72	4.69	4.65	4.72	4.62	4.84	4.60	4.73	5.66	5.66	5.44	5.45	5.57	3.67	4.03	3.59	3.51	3.83	3.70
Mn	0.05	0.04	0.04	0.05	0.05	0.03	0.03	0.03	0.05	0.04	0.10	0.06	0.05	0.02	0.02	0.03	0.02	0.03	0.03
Mg	0.03	0.01	0.02	0.03	0.03	0.04	0.02	0.05	0.09	0.09	0.11	0.07	0.07	0.74	0.83	0.74	0.84	0.80	0.78
Ca	0.05	0.02	0.02	0.02	0.02	0.02	/	0.01	0.01	0.01	0.01	0.02	0.06	0.01	0.01	0.02	0.02	0.01	0.01
Na	0.05	0.03	0.04	0.04	0.03	0.04	0.02	0.09	0.04	0.03	0.04	0.04	0.02	0.09	0.05	0.05	0.07	0.06	0.03
K	2.01	2.01	2.03	1.98	1.93	1.84	2.12	2.02	0.02	0.01	0.01	0.02	0.01	2.10	1.75	2.10	1.83	2.08	2.08
I_{Fe}	0.99	1.00	1.00	0.99	0.99	0.99	1.00	0.99	0.98	0.98	0.98	0.99	0.99	0.83	0.83	0.83	0.81	0.83	0.83
I_{Mg}	0.01	/	/	0.01	0.01	0.01	/	0.01	0.02	0.02	0.02	0.01	0.01	0.17	0.17	0.17	0.19	0.17	0.17
T (°C)	409	376	419	422	434	480	592	549	/	/	/	/	/	670	664	686	670	686	693

$I_{Fe} = Fe^{2+}/(Fe^{2+} + Mg)$, $I_{Mg} = Mg/(Fe^{2+} + Mg)$.

4.3. Zircon U-Pb Geochronology

LA–ICP–MS U–Pb dating results are listed in Table 3. Fifteen zircon grains were analyzed for sample HZ12A. Four analyses deviated from concordia, indicating a late Pb loss due to subsequent tectonothermal event(s). Ten spots yielded a coherent group with the $^{206}Pb/^{238}U$ weighted mean age of 141 ± 3 Ma (MSWD = 0.8) (Figure 7a), interpreted as the crystallization age of the sample. One older spot analysis was calculated as 244 Ma, likely representing the age of inherited or captured zircons. Nineteen grains were analyzed for sample HZ13A. Six spots deviated from concordia, suggestive of a Pb loss due to subsequent tectonothermal event(s). Ten analyses yielded a coherent group with the $^{206}Pb/^{238}U$ weighted mean age of 141 ± 4 Ma (MSWD = 0.43) (Figure 7b), interpreted as the crystallization age of the sample. Three older spots were calculated as 732 Ma, 502 Ma, and 244 Ma, respectively, likely representing the ages of inherited or captured zircons.

Table 3. LA–ICP–MS zircon U-Pb isotopic analyses of the granites from the Xinlu pluton.

Spot	Isotope Ratio						Age (Ma)			
	$^{207}Pb/^{206}Pb$	±1 σ	$^{207}Pb/^{235}U$	±1 σ	$^{206}Pb/^{238}U$	±1 σ	$^{207}Pb/^{235}U$	±1 σ	$^{206}Pb/^{238}U$	±1 σ
HZ12A fine-grained granite										
1	0.0473	0.002	0.1453	0.01	0.0222	0.0009	138	6	142	6
2	0.0518	0.002	0.1612	0.01	0.0225	0.0007	152	5	144	4
3	0.0527	0.002	0.1000	0.00	0.0137	0.0004	97	3	88	3
4	0.0531	0.002	0.1203	0.00	0.0164	0.0005	115	4	105	3
5	0.0522	0.002	0.1617	0.01	0.0225	0.0007	152	5	143	4
6	0.0512	0.002	0.1487	0.01	0.0211	0.0007	141	4	134	4
7	0.0555	0.004	0.2778	0.02	0.0386	0.0039	249	14	244	24
8	0.0508	0.002	0.1508	0.00	0.0215	0.0006	143	4	137	4
9	0.0545	0.002	0.1729	0.01	0.0230	0.0007	162	5	147	4
10	0.0498	0.002	0.1551	0.00	0.0226	0.0007	146	4	144	4
11	0.0514	0.002	0.1560	0.01	0.0222	0.0007	147	4	141	5
12	0.0525	0.002	0.1618	0.01	0.0224	0.0007	152	5	143	4
13	0.0531	0.002	0.1255	0.01	0.0171	0.0006	120	5	109	4
14	0.0530	0.002	0.1075	0.00	0.0147	0.0007	104	3	94	4
15	0.0512	0.002	0.1517	0.00	0.0215	0.0006	143	4	137	4
HZ13A coarse-grained granite										
1	0.0589	0.007	0.1606	0.02	0.0221	0.0026	151	18	141	16
2	0.0632	0.021	0.0827	0.01	0.0100	0.0017	81	14	64	11
3	0.0589	0.002	0.1775	0.01	0.0226	0.0009	166	5	144	6
4	0.0530	0.002	0.1497	0.01	0.0223	0.0016	142	5	142	10
5	0.0561	0.004	0.1663	0.01	0.0221	0.0017	156	12	141	10
6	0.0602	0.002	0.0861	0.00	0.0104	0.0003	84	3	66	2
7	0.0516	0.003	0.1146	0.01	0.0161	0.0011	110	10	103	7
8	0.0520	0.002	0.0994	0.00	0.0139	0.0005	96	3	89	3
9	0.0581	0.007	0.6587	0.09	0.0810	0.0034	514	55	502	20
10	0.0536	0.003	0.1581	0.01	0.0220	0.0012	149	9	140	7
11	0.0520	0.002	0.1597	0.01	0.0222	0.0007	150	5	142	5
12	0.0532	0.007	0.2748	0.04	0.0386	0.0041	247	32	244	26
13	0.0589	0.006	0.1748	0.02	0.0221	0.0018	164	19	141	11
14	0.0484	0.002	0.1527	0.01	0.0228	0.0008	144	5	145	5
15	0.0509	0.002	0.1589	0.01	0.0226	0.0007	150	4	144	4
16	0.0589	0.003	0.1153	0.01	0.0142	0.0010	111	5	91	6
17	0.0625	0.004	1.0321	0.07	0.1203	0.0082	720	37	732	47
18	0.0503	0.002	0.0908	0.00	0.0130	0.0004	88	3	83	3
19	0.0608	0.002	0.1776	0.01	0.0211	0.0007	166	5	135	4

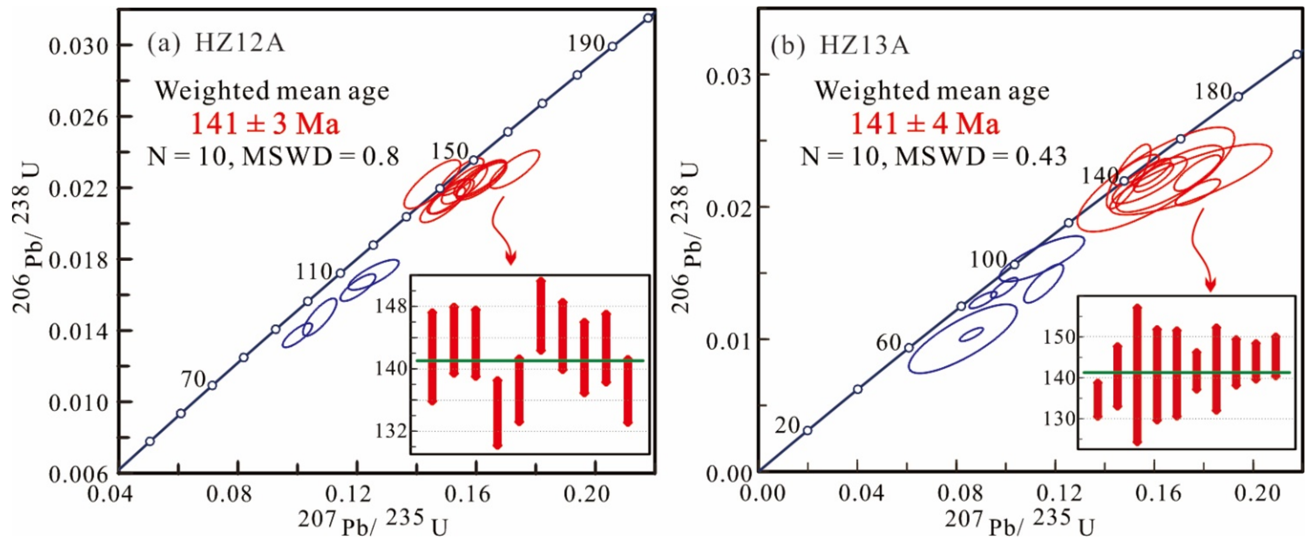

Figure 7. Zircon U-Pb age concordia diagrams of the fine-grained biotite granite (**a**) and coarse-grained porphyritic potassium granite (**b**) from the Xinlu pluton.

5. Discussion

5.1. Formation Age of the Huashan–Guposhan Pluton

The South China Craton is characterized by widespread Mesozoic igneous rocks and coeval large-scale W-Sn polymetallic mineralization [29,46]. The Huashan–Guposhan pluton, an important part of Mesozoic igneous rocks in the South China Craton, consists of a series of small plutons such as Xinlu pluton, Niumiao pluton, and Lisong pluton (Figure 2). Previous studies have conducted some geochronological work on these plutons and have shown that the major formation age is Jurassic. For instance, the Huashan and Wuyangshan plutons were considered to be formed during the early Yanshanian, whereas the other small plutons intruded during the late Yanshanian [31]. Detailed geochronological studies have shown that the Huashan pluton formed at 162 ± 1 Ma, the Niumiao pluton formed at 163 ± 4 Ma, and the Tong'an pluton formed at 160 ± 4 Ma (SHRIMP zircon U-Pb age), whereas the Yinping pluton formed at 148 ± 4 Ma (LA–ICPMS zircon U-Pb age) [27,47,48]. The Guposhan and Lisong plutons in the eastern part of the Huashan–Guposhan pluton were also regarded as being formed in the Jurassic (165-162 Ma) (Table 4; [15,27]).

Table 4. Geochronological data of igneous rocks from the Huashan–Guposhan pluton.

Pluton	Age (Ma)	Method	Reference
Xinlu pluton	141 ± 3, 141 ± 4	LA–ICPMS zircon U-Pb	This study
Huashan pluton	151 ± 7	LA–ICPMS zircon U-Pb	[27]
	165	Rb-Sr isochron	[47]
	162 ± 1	SHRIMP zircon U-Pb	[26,27]
Guposhan pluton	163 ± 4	LA–ICPMS zircon U-Pb	[27]
	161 ± 2, 165 ± 2	LA–ICPMS zircon U-Pb	[15]
Niumiao pluton	163 ± 4	SHRIMP zircon U-Pb	[14]
	161	Hornblende Ar/Ar	[48]
Tong'an pluton	160 ± 4	SHRIMP zircon U-Pb	[14]
	163	Hornblende Ar/Ar	[48]
Yingping pluton	148 ± 4	LA–ICPMS zircon U-Pb	[27]
Lisong pluton	163 ± 1	LA–ICPMS zircon U-Pb	[15]
	162 ± 2, 162 ± 3	SHRIMP zircon U-Pb	[27]
Dark enclaves	162 ± 2	SHRIMP zircon U-Pb	[26,27]

In this study, zircon LA–ICP–MS U-Pb analysis results showed that two granite samples from the Xinlu pluton yielded formation ages of 141 ± 3 Ma and 141 ± 4 Ma, respectively. This indicates that early Cretaceous magmatism, in addition to the Jurassic magmatism, occurred in the Huashan–Guposhan areas in Northeast Guangxi.

5.2. Rock Type

Granite can be subdivided genetically into A-, S-, I-, and M-types according to their protolith nature [49]. These different types of granite have been widely studied because of their special compositions and particular tectonic settings [49–53].

Lithologically, there were no aluminum-rich minerals (e.g., garnet) in both fine- and coarse-grained granite samples from the Xinlu pluton, in contrast to S-type granites that usually contain aluminum-rich minerals and aluminum enclaves [51]. Scarce occurrence of hornblende in these samples suggests that they are different from I-type granites [50,51,54]. Chemically, the granites of the Xinlu pluton showed very low P_2O_5 contents (Table 1) and are mostly metaluminous (Figure 4a), in contrast to S-type granites that are high in P_2O_5 contents and strongly peraluminous [53,55]. They showed obvious negative Eu, Sr, and Ba anomalies (Figure 6) and had high 10,000 × Ga/Al ratios and (Zr + Nb + Ce + Y) contents. These geochemical characteristics were similar to A-type granites but were different from I-type granites [50,54,56–59]. In addition, the obviously high HREE and HFSE (high field strength elements, e.g., Ga, Y, Zr, Nb) concentrations and (K_2O + Na_2O)/CaO ratios of the granites from the Xinlu pluton further indicated that they belong to A-type granites [33]. In the Nb versus 10,000 × Ga/Al diagram [51], the samples plot in the A-type granite field (Figure 8a).

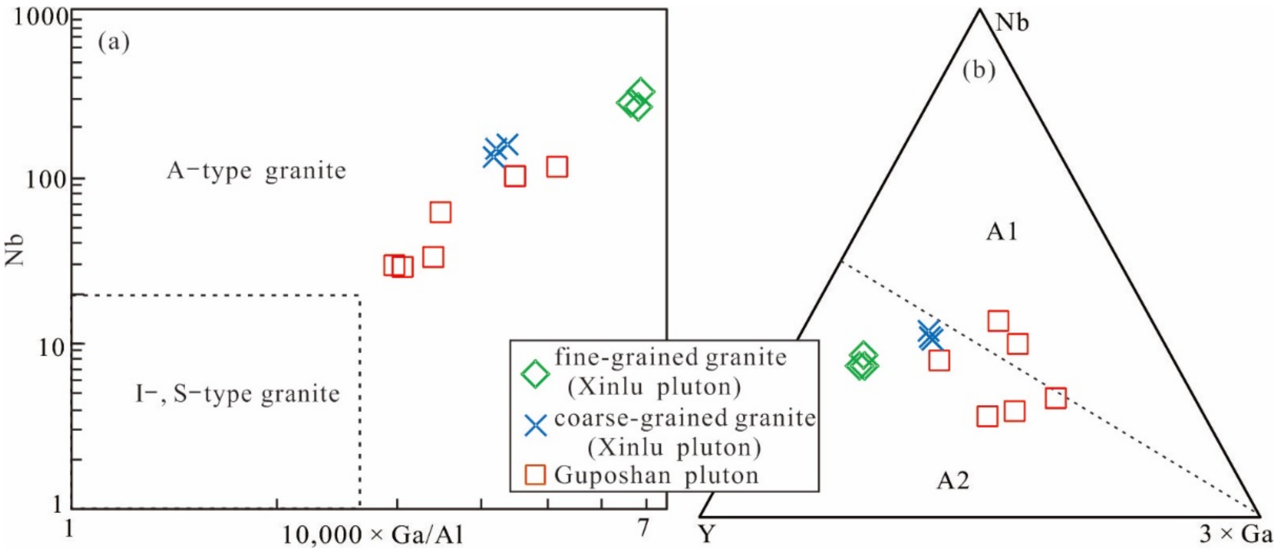

Figure 8. Plots of (**a**) 10,000 × Ga/Al versus Nb and (**b**) Nb-Y-3 × Ga for the granites from the Xinlu and Guposhan plutons.

It is worth noting that the fine- and coarse-grained granites showed different geochemical characteristics (Table 1, Figure 6). This indicates that their magma source has undergone different degrees of fractional crystallization.

Taking the above mineralogical and geochemical evidence into consideration, the granites from the Xinlu pluton likely belong to A-type granite.

A-type granites can be further divided into two chemical types, namely, A1- and A2-types, which showed obviously different sources and tectonic settings [50]. The A1-type granite was characterized by trace element ratios and magma sources similar to those observed for OIB (oceanic-island basalts) [50]. This type always emplaces in continental rifts or during intraplate magmatism [50]. The A2-type granite is distinguished by trace element ratios that vary from those observed for island-arc basalts (IAB) to those observed for continental crust [50]. This type represents magmas originated from continental crust or underplated crust that has been through a cycle of continent–continent collision or island-arc magmatism [50]. Y/Nb, Ce/Nb, and Yb/Ta ratios of the granite samples from the Xinlu pluton were similar to A2-type granites. In the Nb-Y-3 × Ga diagram [50], the granites plot in the A2-type field (Figure 8b), further implying that they belong to A2-type granites.

5.3. Tectonic Significance

Zircon LA–ICP–MS U-Pb analysis of this study shows that the granites from the Xinlu pluton formed at ca. 141 Ma, indicating that Early Cretaceous magmatism existed in the northeastern part of Guangxi. Actually, regional geological data have shown that extensive Mesozoic magmatism occurred in South China. These Mesozoic igneous rocks mainly formed at 195–170 Ma, 170–155 Ma, 140–120 Ma, and 110–90 Ma [5,21,29,60–67].

In addition, two stages of early Mesozoic fold structures have been identified in South China, i.e., early EW-trending fold system and late NNE-trending fold system [68]. These two superimposed fold systems record two different tectonic compressional events, i.e., far-field effects of the Indosinian collisional orogeny and the northwestward low-angle subduction of the Paleo-Pacific plate during the early Yanshanian (ca. 170 Ma) [68,69]. This indicates that the transition time between the Indosinian tectonic regime and the Paleo-Pacific tectonic regime in South China likely occurred at ca. 170 Ma. This means that low-angle subduction of the Paleo-Pacific plate underneath the Eurasian plate took place at ca. 170 Ma [5,21,48,64–67]. At the same time, tectonics and magmatism of South China began to be dominated by the Paleo-Pacific tectonic regime, which resulted in numerous middle-late Jurassic (170–155 Ma) igneous rocks and NNE-trending fold systems in South China [21,60,61]. The subduction angle of the Paleo-Pacific plate slowly increased after ca. 155 Ma [21,70,71]. However, detailed timing of the increased subduction angle is still unclear.

In this study, ≈141 Ma granites were identified in the northeastern part of Guangxi (Figure 7). The granites were enriched in large ion lithophile elements (LILE, e.g., Rb, K) and showed no obvious negative Nb-Ta anomalies (Figure 6a). These geochemical features are different from typical "island arc" igneous rocks. So far, there is no evidence that island arc magmatism or ophiolite has been observed in inland areas of South China during the early Cretaceous [21,29,72,73]. Therefore, the Xinlu pluton is unlikely to have formed in an island arc environment. The granite samples belong to A2-type granites, which commonly represent post-collision or back-arc extensional environment [50,51]. In addition, in eastern and central South China, voluminous Cretaceous (140–120 Ma) volcanic rocks occurred in the Cretaceous extensional basins that were regarded as resulting from back-arc extension [70,74]. In the Rb versus Y + Nb and Ta versus Yb discriminant diagrams [75], the granites plot in the within plate granite field (Figure 9). The above evidence suggests that the granites in this study formed in an extensional environment, probably in a back-arc extensional setting. Combined with the widespread 135–92 Ma A-type granites [60–62] and 140–120 Ma igneous rock belt in Southeast Coastal Areas in South China [5,21,29,74], we propose that the increased subduction angle of the Paleo-Pacific plate might have occurred at ca. 141 Ma.

Taking the above into account, the granites in this study likely formed in a back-arc extensional environment in response to the increased subduction angle of the Paleo-Pacific plate during the early Cretaceous (ca. 141 Ma).

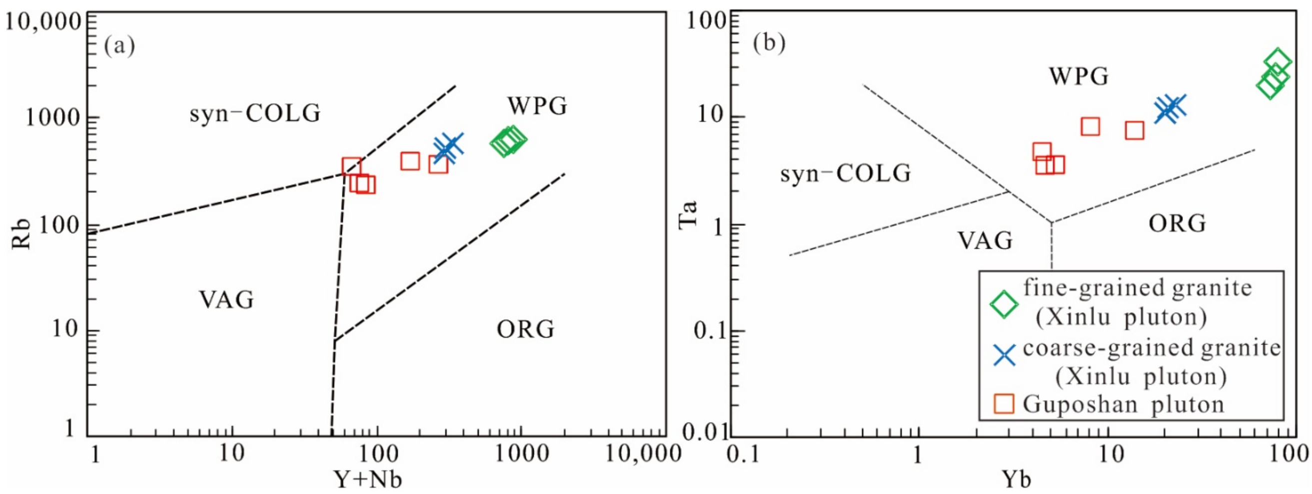

Figure 9. Plots of (**a**) Rb versus Y + Nb and (**b**) Ta versus Yb for the granites from the Xinlu and Guposhan plutons. Abbreviations: WPG, within plate granite; syn-COLG, syn-collision granite; VAG, volcanic arc granite; ORG, ocean ridge granite.

5.4. Granitic Magmatism and REE Mineralization

Trace element analysis results show that the granites from the Xinlu pluton had high REE contents (>451 ppm), but LREE and HREE contents were significantly different in different types of granites (Table 1). The fine-grained granites were characterized by higher HREE contents (ΣHREE = 797–864 ppm), lower LREE contents (ΣLREE = 146–166 ppm), and lower LREE/HREE ratios (0.18–0.19) than the coarse-grained granites (ΣHREE = 262–297 ppm, ΣLREE = 189–212 ppm, LREE/HREE = 0.71–0.72) (Figure 6b). These characteristics are generally similar to the granites from the south Jiangxi province, where HREE deposits are widespread (Table 5; [76–78]). This indicates that the Xinlu pluton shows good HREE mineralization potential. Previous studies have shown that HREE-rich granites are characterized by high SiO_2 contents and high degrees of magma crystallization and differentiation [55,76,79]. All the granite samples display high SiO_2 contents (>72 wt %) (Table 1); extremely negative Sr, Ba, and Eu anomalies (Figure 6); and a linear relationship between SiO_2 contents and some major oxides (Figure 5b,d,f), suggesting that high degrees of magma differentiation occurred during the process of magma evolution. Early crystallization of LREE-rich minerals (e.g., allanite, titanite, and monazite) can lead to relative enrichment in HREE in the residual melt [76]. In the plots of SiO_2 versus REE (Figure 10), ΣHREE showed a negative correlation with SiO_2 contents, whereas ΣLREE had a positive correlation with SiO_2 contents. These data indicate that magma differentiation might have played an important role in REE enrichment and that different REE contents in the fine- and coarse-grained granites may be a result of crystallization and differentiation.

Table 5. REE contents of the Xinlu pluton and some representative granites related to REE deposits in Jiangxi province, South China.

Pluton	Rock Type	LREE (ppm)	HREE (ppm)	REE (ppm)	LREE/HREE	References
Xinlu	fine-grained granite	156	832	988	0.19	This study
Xinlu	coarse-grained granite	198	277	475	0.72	This study
Zhaibei	fine-grained muscovitic alkali-feldspar granite	53	140	194	0.4	[76]
Zhaibei	coarse-grained biotite syenogranite	276	112	389	2.86	[76]
Zudong	medium-grained granite	84.5	179	264	0.52	[80]
Dabu	fine-grained granite	58	141	199	0.46	[80]
Dabu	medium-grained granite	128	149	278	1.26	[80]

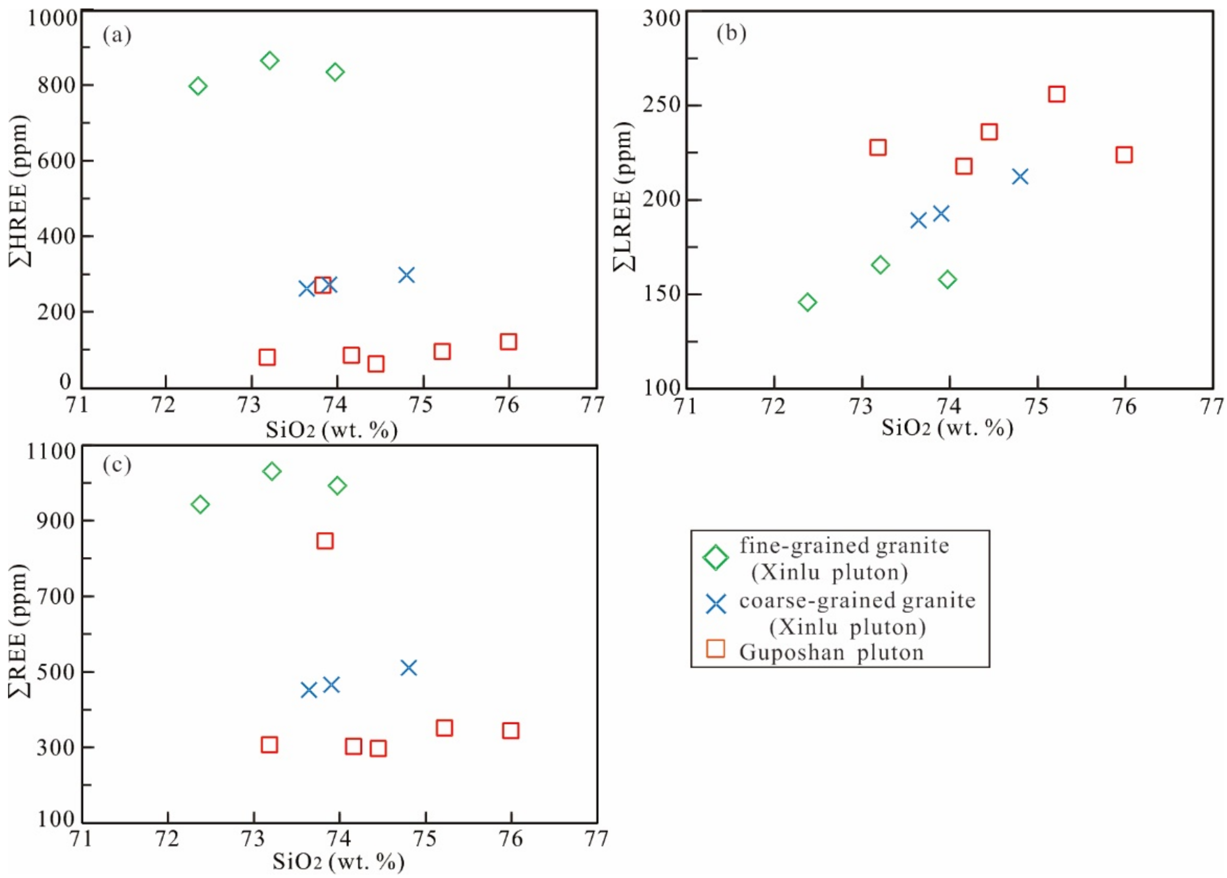

Figure 10. Plots of SiO_2 versus (**a**) ΣHREE, (**b**) ΣLREE, and (**c**) ΣREE for the granites from the Xinlu and Guposhan plutons.

Biotite is the most common mafic mineral in granite and generally shows higher REE contents relative to other rock-forming minerals in granite. It thus becomes an ideal indicator to reveal the relationship between granitic magmatism and REE mineralization. Previous studies have shown that the compositions of biotite can be used to estimate formation temperature of biotite [81]. Henry et al. (2005) further proposed a formula to calculate the formation temperature of biotites [82]. The results show that biotites from the Guposhan pluton had a crystallization temperature of 664–693 °C (average = 678 °C) (Table 2), whereas biotites from the fine-grained granites showed a much lower temperature (376–592 °C; average = 460 °C). In view of the biotites from the fine-grained granites showing the features of alteration as evidenced by chloritization and epidotization (Figure 3c) and low TiO_2 and MgO contents ([83]; Table 2, Figure 11), the temperature of 376–592 °C likely represents the temperature of hydrothermal alteration. REE minerals, such as thorite, bastnasite, thorite-(Y), and synchysite-(Y), can be formed during hydrothermal alteration [76]. These hydrothermal REE minerals are easily weathered and thus become important suppliers of ion-exchangeable REEs in regolith [84–86]. Therefore, hydrothermal alteration might have played an important role in REE mineralization of the Xinlu pluton.

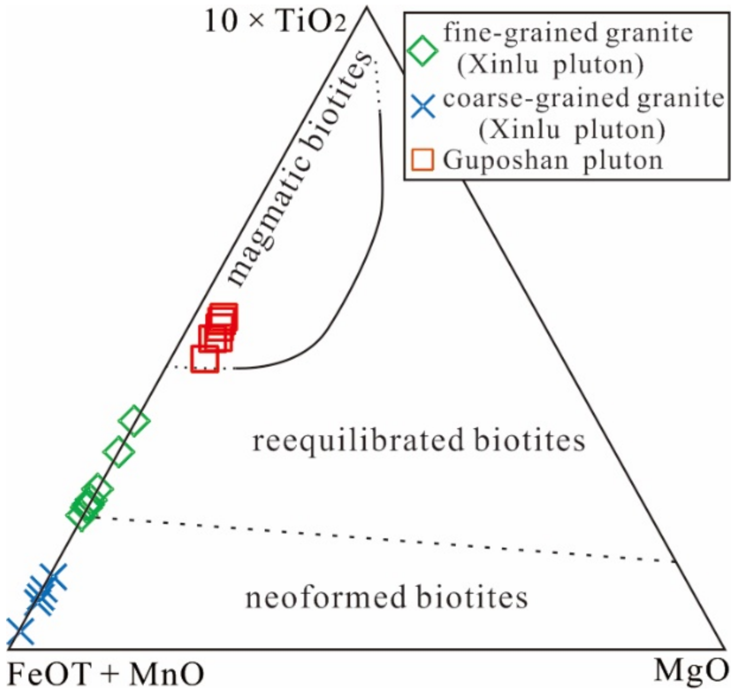

Figure 11. Plot of 10 × TiO_2-FeOT + MnO-MgO for the biotites of the granites from the Xinlu and Guposhan plutons.

6. Conclusions

(1) LA–ICP–MS zircon U–Pb dating results showed that granites from the Xinlu pluton in northeastern Guangxi signaled an early Cretaceous age (ca. 141 Ma), indicating that early Cretaceous magmatism occurred in inland areas of South China.

(2) The granites belong to A-type granite and likely formed in a back-arc extensional environment in response to the increased subduction angle of the Paleo-Pacific plate.

(3) They had high REE contents (>451 ppm), especially the fine-grained granites showing higher HREE contents, lower LREE contents, and lower LREE/HREE ratios than the coarse-grained granites.

(4) Strong hydrothermal alteration and magma differentiation, which can affect activation and mobilization of REE, might have played an important role in REE enrichment.

Author Contributions: Conceptualization, Y.Q. and Y.C.; methodology, Z.H. (Zhixuan Han), P.L. and C.L.; software, Y.Z. (Yongshan Zhao); validation, W.F.; formal analysis, Y.C.; investigation, Z.H. (Zhixuan Han), P.L., C.L. and Y.C.; resources, W.F. and Y.Z. (Yun Zhou); data curation, Y.Z. (Yongshan Zhao), Z.H. (Zhengchao Han) and Y.C.; writing—original draft preparation, Y.Q. and Y.C.; writing—review and editing, Y.Z. (Yun Zhou) and Y.C.; visualization, Y.Z. (Yun Zhou); supervision, Y.Z. (Yun Zhou); project administration, W.F. and Y.Z. (Yun Zhou); funding acquisition, Y.Z. (Yun Zhou). All authors have read and agreed to the published version of the manuscript.

Funding: This research was funded by the Guangxi Key R&D Program (Guike AB22035045), the Guangxi Natural Science Foundation Program (2020GXNSFGA297003, 2022GXNSFAA035620), the National Natural Science Foundation of China (42072259, 92055208), and the Open Fund of Guangdong Provincial Key Lab of Geodynamics and Geohazards (KLGG201906).

Institutional Review Board Statement: Not applicable.

Informed Consent Statement: Not applicable.

Data Availability Statement: Not applicable.

Acknowledgments: We are grateful to Editors and reviewers for their critical and constructive comments and suggestions on this paper. We thank Hongxia Yu and Zhenglin Li for their assistance in helping with the geochemical and isotopic analyses.

Conflicts of Interest: The authors declare no conflict of interest.

References

1. Xu, F.; Zhang, G.L.; Yan, W.; Zhang, J.; Yao, J.H. Subduction of the paleo-Pacific plate recorded by arc volcanism in the South China Sea margin. *Gondwana Res.* **2022**, *110*, 58–72. [CrossRef]
2. Qiu, L.; Li, X.; Li, X.W.; Yan, D.P.; Ren, M.H.; Zhang, L.L.; Cheng, G.S. Petrogenesis of early cretaceous intermediate to felsic rocks in Shanghai, South China: Magmatic response to Paleo-Pacific plate subduction. *Tectonophysics* **2022**, *838*, 229469. [CrossRef]
3. Zhao, L.; Guo, F.; Zhang, X.B.; Wang, G.Q. Cretaceous crustal melting records of tectonic transition from subduction to slab rollback of the Paleo-Pacific Plate in SE China. *Lithos* **2021**, *384–385*, 105985. [CrossRef]
4. Wang, Q.; Li, J.W.; Jian, P.; Zhao, Z.H.; Xiong, X.L.; Bao, Z.W.; Xu, J.F.; Li, C.F.; Ma, J.L. Alkaline syenites in eastern Cathaysia (South China): Link to Permian-Triassic transtension. *Earth Planet. Sci. Lett.* **2005**, *230*, 339–354. [CrossRef]
5. Zhou, X.; Sun, T.; Shen, W.; Shu, L.; Niu, Y. Petrogenesis of Mesozoic granitoids and volcanic rocks in South China: A response to tectonic evolution. *Episodes* **2006**, *29*, 26–33. [CrossRef]
6. Li, Z.X.; Li, X.H. Formation of the 1300-km-wide intracontinental orogeny and postorogenic magmatic province in Mesozoic South China: A flat-slab subduction model. *Geology* **2007**, *35*, 179–182. [CrossRef]
7. Deng, J.; Yang, X.Y.; Zartman, R.E.; Qi, H.; Qi, H.S.; Zhang, L.P.; Liu, H.; Zhang, Z.F.; Mastoi, A.S.; Berador, A.E.G.; et al. Early Cretaceous transformation from Pacific to Neo-Tethys subduction in the SW Pacific Ocean: Constraints from Pb-Sr-Nd-Hf isotopes of the Philippine arc. *Geochim. Cosmochim. Acta* **2020**, *285*, 21–40. [CrossRef]
8. Sun, W.D.; Ding, X.; Hu, Y.H.; Li, X.H. The golden transformation of the Cretaceous plate subduction in the west Pacific. *Earth Planet. Sci. Lett.* **2007**, *262*, 533–542. [CrossRef]
9. Koppers, A.A.P.; Morgan, J.P.; Morgan, J.W.; Staudigel, H. Testing the fixed hotspot hypothesis using $^{40}Ar/^{39}Ar$ age progressions along seamount trails. *Earth Planet. Sci. Lett.* **2001**, *185*, 237–252. [CrossRef]
10. Sharp, W.D.; Clague, D.A. 50-Ma initiation of Hawaiian-Emperor bend records major change in Pacific plate motion. *Science* **2006**, *313*, 1281–1284. [CrossRef]
11. Zhu, J.C.; Zhang, P.H.; Xie, C.F.; Zhang, H.; Yang, C. Magma mixing origin of the mafic enclaves in Lisong Granite, NE Guangxi, western Nanling Mountains. *Geochimica* **2006**, *35*, 506–516. (In Chinese with English Abstract)
12. Zhao, K.D.; Jiang, S.Y.; Zhu, J.C.; Li, L.; Dai, B.Z.; Jiang, Y.H.; Ling, H.F. Hf isotopic composition of zircons from the Huashan-Guposhan intrusive complex and their mafic enclaves in northeastern Guangxi: Implication for petrogenesis. *Chin. Sci. Bull.* **2009**, *6*, 509–519. [CrossRef]
13. Li, X.F.; Feng, Z.H.; Xiao, R.; Song, C.A.; Yang, F.; Wang, C.Y.; Kang, Z.Q.; Mao, W. Spatial and Temporal Distributions and the Geological Setting of the W-Sn-Mo-Nb-Ta Deposits at the Northeast Guangxi, Southe China. *Acta Geol. Sin.* **2012**, *86*, 1714–1725. (In Chinese with English Abstract)
14. Zhu, J.C.; Xie, C.F.; Zhang, P.H.; Yang, C.; Gu, S.Y. Niumiao and Tong'an intrusive bodies of NE Guangxi: Petrology zircon SHRIMP U-Pb geochronology and geochemistry. *Acta Petrol. Sin.* **2005**, *21*, 665–676. (In Chinese with English Abstract)
15. Gu, S.Y.; Hua, R.M.; Qi, H.W. Study on Zircon LA-ICP-MS U-Pb Dating and Sr-Nd Isotope of the Guposhan Granite in Guangxi. *Acta Geol. Sin.* **2006**, *80*, 543–553. (In Chinese with English Abstract) [CrossRef]
16. Shu, X.J.; Wang, X.L.; Sun, T.; Chen, W.F.; Shen, W.Z. Crustal formation in the Nanling Range, South China Block: Hf isotope evidence of zircons from Phanerzoic granitoids. *J. Asian Earth Sci.* **2013**, *74*, 210–224. [CrossRef]
17. Cai, Y.F.; Wang, Y.J.; Cawood, P.A.; Fan, W.M.; Liu, H.C.; Xing, X.W.; Zhang, Y.Z. Neoproterozoic subduction along the Ailaoshan zone, South China: Geochronological and geochemical evidence from amphibolite. *Precambrian Res.* **2014**, *245*, 13–28. [CrossRef]
18. Cai, Y.F.; Wang, Y.J.; Cawood, P.A.; Zhang, Y.Z.; Zhang, A.M. Neoproterozoic crustal growth of the Southern Yangtze Block: Geochemical and zircon U-Pb geochronological and Lu-Hf isotopic evidence of Neoproterozoic diorite from the Ailaoshan zone. *Precambrian Res.* **2015**, *266*, 137–149. [CrossRef]
19. Cai, Y.F.; Liu, H.C.; Feng, Z.H.; Zhou, Y.; Liu, X.J.; Wang, Z.L.; Ma, L.Y.; Li, Z.L.; Xu, J.F. Neoproterozoic active margin of the SW South China Block: Constraints from U-Pb ages, Sr-Nd isotopes and geochemical data for the gabbro and granodiorite along the Ailaoshan tectonic belt. *Lithos* **2020**, *358–359*, 105387. [CrossRef]
20. Zhou, Y.; Liang, X.Q.; Wu, S.C.; Cai, Y.F.; Liang, X.R.; Shao, T.B.; Wang, C.; Fu, J.G.; Jiang, Y. Isotopic geochemistry, zircon U–Pb ages and Hf isotopes of A-type granites from the Xitian W–Sn deposit, SE China: Constraints on petrogenesis and tectonic significance. *J. Asian Earth Sci.* **2015**, *105*, 122–139. [CrossRef]
21. Zhou, Y.; Liang, X.Q.; Kröner, A.; Cai, Y.F.; Shao, T.B.; Wen, S.N.; Jiang, Y.; Fu, J.G.; Wang, C.; Dong, C.G. Late Cretaceous lithospheric extension in SE China: Constraints from volcanic rocks in Hainan Island. *Lithos* **2015**, *232*, 100–110. [CrossRef]
22. Wang, Y.J.; Fan, W.M.; Zhang, G.W.; Zhang, Y.H. Phanerozoic tectonics of the South China Block: Key observations and controversies. *Gondwana Res.* **2013**, *23*, 1273–1305. [CrossRef]
23. Liu, H.C.; Xia, X.P.; Lai, C.K.; Gan, C.S.; Zhou, Y.; Huangfu, P.P. Break–away of South China from Gondwana: Insights from the Silurian high–Nb basalts and associated magmatic rocks in the Diancangshan–Ailaoshan fold belt (SW China). *Lithos* **2018**, *318–319*, 194–208. [CrossRef]
24. Zhou, Y.; Sun, S.Y.; Feng, Z.H.; Xu, C.; Cai, Y.F.; Liang, X.Q.; Liu, X.J.; Du, Y.J. A new insight into the eastern extension of the Proto-Tethyan margin of Gondwana by Early Paleozoic volcanic rocks in South China. *Lithos* **2021**, *398–399*, 106328. [CrossRef]

25. Feng, Z.H.; Wang, C.Z.; Liang, J.C.; Li, J.Z.; Huang, Y.G.; Liao, J.F.; Wang, R. The emplacement mechanisms and growth styles of the Guposhan-Huashan batholith in western Nanling Range, South China. *Sci. China Earth Sci.* **2011**, *54*, 45–60. (In Chinese with English Abstract) [CrossRef]
26. Zhu, J.C.; Zhang, P.H.; Xie, C.F.; Zhang, H.; Yang, C. The Huashan-Guposhan A-type granitoid belt in the western part of the Nanling Mountains: Petrology, geochemistry and genetic interpretations. *Acta Geol. Sin.* **2006**, *80*, 529–542. (In Chinese with English Abstract)
27. Zhu, J.C.; Zhang, P.H.; Xie, C.F.; Zhang, H.; Yang, C. Zircon U-Pb age framework of Huashan-Guposhan intrusive belt, western part of Nanling Range, and its geological significance. *Acta Petrol. Sin.* **2006**, *22*, 2270–2278. (In Chinese with English Abstract)
28. Wang, R.C.; Xie, L.; Chen, J.; Yu, A.P.; Wang, L.B.; Lu, J.J.; Zhu, J.C. Tin-carrier minerals in metaluminous granites of the western Nanling Range (southern China): Constraints on processes of tin mineralization in oxidized granites. *J. Asian Earth Sci.* **2013**, *74*, 361–372. [CrossRef]
29. Cai, Y.F.; Feng, Z.H.; Shao, T.B.; Hu, R.G.; Zhou, Y.; Xu, J.F. New precise zircon U-Pb and muscovite ^{40}Ar-^{39}Ar geochronology of the Late Cretaceous W-Sn mineralization in the Shanhu orefield, South China. *Ore Geol. Rev.* **2017**, *84*, 338–346. [CrossRef]
30. Yu, Y.; Li, X.F.; Xiao, R.; Mao, W.; Jia, Y.Z. Zircon LA-ICP-MS U-Pb and Sericite ^{40}Ar/^{39}Ar Ages at Shanhu W-Sn Deposit, Guangxi Province, China, and its Implications for W-Sn Minerlization. *Acta Mineral. Sin.* **2014**, *34*, 297–304. (In Chinese with English Abstract)
31. Feng, Z.H.; Liang, J.C.; Zhang, G.L.; Li, X.F.; Deng, J.X. On the lithodemic units of Mesozoic granitoid in east Guangxi: A case from Guposhan-Huashan granitic pluton. *J. Guilin Inst. Technol.* **2002**, *22*, 333–340. (In Chinese with English Abstract)
32. Lu, X.P.; Lu, X.Z.; Geng, M.W.; Lu, Q.F.; Shi, S.D. Geological characteristics and genesis of the Guposhan tin orefield in Guangxi. *Geol. Miner. Resour. South China* **2005**, *2*, 53–60. (In Chinese with English Abstract)
33. Feng, Z.H. Emplacement Process and Structural Analysis of Gupushan-Huashan Granitic Pluton, Guangxi. Ph.D. Thesis, Central South University, Changsha, China, 2003. (In Chinese with English Abstract)
34. Cai, Y.F.; Liu, F.L.; Feng, Z.H.; Zhou, Y.; Zeng, C.Y. Mineral Compositional and Chronological Characteristics of Guposhan Pluton in Guangxi and Its Petrogenetic and Metallogenic Significance. *J. Jilin Univ.* **2020**, *50*, 842–856. (In Chinese with English Abstract)
35. Cai, Y.F.; Ma, Y.C.; Zhou, Y.; Su, X.Q.; Feng, Z.H.; Ma, L.H.; Hu, R.G. Characteristics of mineralogy, geochronology and geochemistry of the granite in Huashan, Guangxi and its tectonic implication. *Geol. Explor.* **2018**, *54*, 940–956. (In Chinese with English Abstract)
36. Yuan, H.Q.; Li, S.H.; Cheng, F.; Pei, Q.M.; Zhang, Y.J.; Sun, M.H.; Zhang, H.Y. Weathered material granularity and geochemistry of weathering crust in ion-adsorption type REE deposit: A case from Yangminchong of Guposhan. *J. Guilin Univ. Technol.* **2015**, *35*, 243–250. (In Chinese with English Abstract)
37. Pearce, N.J.G.; Perkins, W.T.; Westgate, J.A.; Gorton, M.P.; Jackson, S.E.; Neal, C.R.; Chenery, S.P. A compilation of new and published major and trace element data for NIST SRM 610 and NIST SRM 612 glass reference materials: Geostandards Newsletter. *J. Geostand. Geoanal.* **1997**, *21*, 115–144. [CrossRef]
38. Black, L.P.; Kamo, S.L.; Allen, C.M.; Aleinikoff, J.N.; Davis, D.W.; Korsch, R.J.; Foudoulis, C. TEMORA 1: A new zircon standard for Phanerozoic U-Pb geochronology. *Chem. Geol.* **2003**, *200*, 155–170. [CrossRef]
39. Yuan, H.L.; Gao, S.; Liu, X.M.; Li, H.M.; Günther, D.; Wu, F.Y. Accurate U-Pb age and trace element determinations of zircon by laser ablation-inductively coupled plasma-mass spectrometry. *Geostand. Geoanal. Res.* **2004**, *28*, 353–370. [CrossRef]
40. Liu, Y.S.; Hu, Z.C.; Gao, S.; Günther, D.; Xu, J.; Gao, C.G.; Chen, H.H. In situ analysis of major and trace elements of anhydrous minerals by LA-ICP-MS without applying an internal standard. *Chem. Geol.* **2008**, *257*, 34–43. [CrossRef]
41. Ludwig, K.R. User's manual for isoplot 3.0: A geochronological toolkit for Microsoft Excel. *Berkeley Geochronol. Cent. Spec. Publ.* **2003**, *4*, 1–71.
42. Li, X.H.; Qi, C.S.; Liu, Y.; Liang, X.R.; Tu, X.L. Petrogenesis of the Neoproterozoic bimodal volcanic rocks along the western margin of the Yangtze Block: New constraints from Hf isotopes and Fe/Mn ratios. *Chin. Sci. Bull.* **2005**, *50*, 2481–2486. [CrossRef]
43. Liu, Y.; Liu, H.C.; Li, X.H. Simultaneous and Precise Determination of 40 Trace Elements in Rock Samples Using ICP-MS. *Geochimica* **1996**, *25*, 552–558. (In Chinese with English Abstract)
44. Sun, S.S.; McDonough, W.F. Chemical and isotopic systematics of oceanic basalts: Implications for mantle composition and processes. *Geol. Soc. Lond., Spec. Publ.* **1989**, *42*, 313–345. [CrossRef]
45. Rieder, M.; Cavazzini, G.; D'Yakonov, Y.S.; Frank-Kamenetskii, V.A.; Gottardi, G.; Guggenheim, S.; Koval', P.V.; Müller, G.; Neiva, A.M.R.; Radoslovich, E.W.; et al. Nomenclature of the Micas. *Mineral. Mag.* **1999**, *63*, 267–279. [CrossRef]
46. Mao, J.W.; Cheng, Y.B.; Chen, M.H.; Pirajno, F. Major types and time-space distribution of Mesozoic ore deposits in South China and their geodynamic settings. *Miner. Depos.* **2013**, *48*, 267–294.
47. Zhu, J.C.; Li, X.D.; Shen, W.Z.; Wang, Y.X.; Yang, J.D. Sr, Nd and O isotope studies on the genesis of the Huashan granite complex. *Acta Geol. Sin.* **1989**, *63*, 225–235. (In Chinese with English Abstract)
48. Li, X.H.; Chung, S.L.; Zhou, H.W.; Lo, C.H.; Liu, Y.; Chen, C.H. Jurassic intraplate magmatism in southern Hunan-eastern Guangxi: 40Ar/39Ar dating, geochemistry, Sr-Nd isotopes and implications for the tectonic evolution of SE China. *Geol. Soc. Lond. Spec. Publ.* **2004**, *226*, 193–215. [CrossRef]
49. Bonin, B. A-type granites and related rocks: Evolution of a concept, problems and prospects. *Lithos* **2007**, *97*, 1–29. [CrossRef]
50. Eby, G.N. Chemical subdivision of the A-type granitoids: Petrogenetic and tectonic implications. *Geology* **1992**, *20*, 641–644. [CrossRef]

51. Whalen, J.B.; Currie, K.L.; Chappell, B.W. A-type granites: Geochemical characteristics, discrimination and petrogenesis. *Contrib. Mineral. Petrol.* **1987**, *95*, 407–419. [CrossRef]
52. King, P.L.; White, A.J.R.; Chappell, B.W.; Allen, C.M. Characterization and origin of aluminous A-type granites from the Lachlan Fold Belt, Southeastern Australia. *J. Petrol.* **1997**, *38*, 371–391. [CrossRef]
53. Clemens, J.D. S-type granitic magmas–petrogenetic issues, models and evidence. *Earth-Sci. Rev.* **2003**, *61*, 1–18. [CrossRef]
54. Chappell, B.W.; White, A.J. Two contrasting granite types. *Pac. Geol.* **1974**, *8*, 173–174.
55. Chappell, B.W. Aluminium saturation in I- and S-type granites and the characterization of fractionated haplogranites. *Lithos* **1999**, *46*, 535–551. [CrossRef]
56. Collins, W.J.; Beams, S.D.; White, A.J.R.; Chappell, B.W. Nature and origin of A-type granites with particular reference to southeastern Australia. *Contrib. Mineral. Petrol.* **1982**, *80*, 189–200. [CrossRef]
57. Miller, C.F.; McDowell, S.M.; Mapes, R.W. Hot and cold granites? Implications of zircon saturation temperatures and preservation of inheritance. *Geology* **2003**, *31*, 529–532. [CrossRef]
58. Watson, E.B.; Harrison, T.M. Zircon saturation revisited: Temperature and composition effects in a variety of crustal magma types. *Earth Planet. Sci. Lett.* **1983**, *64*, 295–304. [CrossRef]
59. Clemens, J.D.; Holloway, J.R.; White, A.J.R. Origin of an A-type granite: Experimental constraints. *Am. Mineral.* **1986**, *71*, 317–324.
60. Gan, C.S.; Wang, Y.J.; Cai, Y.F.; Liu, H.C.; Zhang, Y.Z.; Song, Q.Q.; Guo, X.F. The petrogenesis and tectonic implication of Wengong intrusion in the Nanling Range. *Earth Sci.* **2016**, *41*, 17–34. (In Chinese with English Abstract)
61. Fu, J.M.; Ma, C.Q.; Xie, C.F.; Zhang, Y.M.; Peng, S.B. Ascertainment of the Jinjiling aluminous A-type granite, Hunan Provice and its tectonic setting. *Geochimica* **2005**, *34*, 215–226. (In Chinese with English Abstract)
62. Jiang, S.Y.; Zhao, K.D.; Jiang, Y.H.; Dai, B.Z. Characteristics and Genesis of Mesozoic A-Type Granites and Associated Mineral Deposits in the Southern Hunan and Northern Guangxi Provinces along the Shi-Hang Belt, South China. *Geol. J. China Univ.* **2008**, *14*, 496–509. (In Chinese with English Abstract)
63. Xiao, E.; Qiu, J.S.; Xu, X.S.; Jiang, S.Y.; Hu, J.; Li, Z. Geochronology and geochemistry of the Yaokeng alkaline granitic pluton in Zhejiang province: Petrogenetic and tectonic implications. *Acta Petrol. Sin.* **2007**, *23*, 1431–1440. (In Chinese with English Abstract)
64. Jiang, Y.H.; Jiang, S.Y.; Zhao, K.D.; Ling, H.F. Petrogenesis of Late Jurassic Qianlishan granites and mafic dykes, Southeast China: Implications for a back-arc extension setting. *Geol. Mag.* **2006**, *143*, 457–474. [CrossRef]
65. Jiang, Y.H.; Jiang, S.Y.; Dai, B.Z. Middle to late Jurassic felsic and mafic magmatism in southern Hunan province, southeast China: Implications for a continental arc to rifting. *Lithos* **2009**, *107*, 185–204. [CrossRef]
66. Hu, J.; Qiu, J.S.; Wang, D.Z.; Wang, R.C.; Zhang, X.L. Comparative Investigations of A-type Granites in the Coastal and the Nanling Inland Areas of SE China, and Their Tectonic Significances. *Geol. J. China Univ.* **2005**, *11*, 404–414. (In Chinese with English Abstract)
67. Qiu, J.S.; Wang, D.Z.; Brent, I.A.M. Geochemistry and petrogenesis of the I- and A-type composite granite masses in the coastal area of Zhejiang and Fujian province. *Acta Petrol. Sin.* **1999**, *15*, 237–246. (In Chinese with English Abstract)
68. Zhang, Y.Q.; Xu, X.B.; Jia, D.; Shu, L.S. Deformation record of the change from Indosinian collision related tectonic system to Yanshanian subduction related tectonic system in South China during the Early Mesozoic. *Earth Sci. Front.* **2009**, *16*, 234–247. (In Chinese with English Abstract)
69. Xu, X.B.; Zhang, Y.Q.; Jia, D.; Shu, L.S.; Wang, R.R. Early Mesozoic geotectonic processes in South China. *Geol. China* **2009**, *36*, 573–593. (In Chinese with English Abstract)
70. Shu, L.S. An analysis of principal features of tectonic evolution in South China Block. *Geol. Bull. China* **2012**, *31*, 1035–1053. (In Chinese with English Abstract)
71. Uyeda, S.; Miyashir, A. Plate tectonics and Japanese-islands: Synthesis. *Geol. Soc. Am. Bull.* **1974**, *85*, 1159–1170. [CrossRef]
72. Wang, Y.J.; Fan, W.M.; Guo, F. Geochemistry of early Mesozoic potassium-rich diorites-granodiorites in Southeastern Hunan Province, South China: Petrogenesis and tectonic implications. *Geochem. J.* **2003**, *37*, 427–448. [CrossRef]
73. Zhu, W.G.; Zhong, H.; Li, X.H.; He, D.F.; Song, X.Y.; Ren, T.; Chen, Z.Q.; Sun, H.S.; Liao, J.Q. The early Jurassic mafic-ultramafic intrusion and A-type granite from northeastern Guangdong, SE China: Age, origin, and tectonic significance. *Lithos* **2010**, *119*, 313–329. [CrossRef]
74. Li, J.H.; Zhang, Y.Q.; Dong, S.W.; Johnston, S.T. Cretaceous tectonic evolution of South China: A preliminary synthesis. *Earth Sci. Rev.* **2014**, *134*, 98–136. [CrossRef]
75. Pearce, J.A.; Harris, N.B.W.; Tindle, A.G. Trace Element discrimination diagrams for the tectonic interpretation of granitic rocks. *J. Petrol.* **1984**, *25*, 956–983. [CrossRef]
76. Zhao, Z.; Wang, D.H.; Bagas, L.; Chen, Z.Y. Geochemical and REE mineralogical characteristics of the Zhaibei Granite in Jiangxi Province, southern China, and a model for the genesis of ion-adsorption REE deposits. *Ore Geol. Rev.* **2022**, *140*, 104579. [CrossRef]
77. Zhao, X.; Li, N.B.; Huizenga, J.M.; Zhang, Q.B.; Yang, Y.Y.; Yan, S.; Yang, W.B.; Niu, H.C. Granitic magma evolution to magmatic-hydrothermal processes vital to the generation of HREEs ion-adsorption deposits: Constraints from zircon texture, U-Pb geochronology, and geochemistry. *Ore Geol. Rev.* **2022**, *146*, 104931. [CrossRef]
78. Huang, Y.F.; He, H.P.; Liang, X.L.; Bao, Z.W.; Tan, W.; Ma, L.Y.; Zhu, J.X.; Huang, J.; Wang, H. Characteristics and genesis of ion adsorption type REE deposits in the weathering crusts of metamorphic rocks in Ningdu, Ganzhou, China. *Ore Geol. Rev.* **2021**, *135*, 104173. [CrossRef]

79. Ishihara, S.; Murakami, H. Fractionated ilmenite-series granites in Southwest Japan: Source magma for REE-Sn-W mineralizations. *Resour. Geol.* **2006**, *56*, 245–256. [CrossRef]
80. Yang, Z.Y.; Liu, Z.; Zhu, X.L. Comparison in the Characteristics and Related Metallogeny between Heavy Rare Earth in Dabu and Zudong, Southern JiangXi, China. *Collect. Pap. Geol. Soc. Jiangxi Prov.* **2020**, *I*, 170–180. (In Chinese with English Abstract)
81. Patiño, D.A.E. Titanium Substitution in Biotite: An Empirical Model with Applications to Thermometry, O_2 and H_2O Barometries, and Consequences for Biotite Stability. *Chem. Geol.* **1993**, *108*, 133–162.
82. Henry, D.J.; Guidotti, C.V.; Thomson, J.A. The Ti-saturation surface for low-to-medium pressure metapelities biotites: Implications for geothermometry and Ti-substitution mechanisms. *Am. Mineral.* **2005**, *90*, 316–328. [CrossRef]
83. Nachit, H.; Ibhi, A.; Abia, E.H.; Ohoud, M.B. Discrimination between primary magmatic biotites, reequilibrated biotites and neoformed biotites. *Comptes Rendus Geosci.* **2005**, *337*, 1415–1420. [CrossRef]
84. Bern, C.R.; Yesavage, T.; Foley, N.K. Ion-adsorption REEs in regolith of the Liberty Hill pluton, South Carolina, USA: An effect of hydrothermal alteration. *J. Geochem. Explor.* **2017**, *172*, 29–40. [CrossRef]
85. Sanematsu, K.; Kon, Y.; Imai, A.; Watanabe, K.; Watanabe, Y. Geochemical and mineralogical characteristics of ion-adsorption type REE mineralization in Phuket, Thailand. *Min. Depos.* **2013**, *48*, 437–451. [CrossRef]
86. Vieira, C.C.; Botelho, N.F.; Garnier, J. Geochemical and mineralogical characteristics of REEY occurrences in the Mocambo Granitic Massif tin-bearing A-type granite, central Brazil, and its potential for ion-adsorption-type REEY mineralization. *Ore Geol. Rev.* **2019**, *105*, 467–486. [CrossRef]